Chinese Chemical Letters 36 (2025) 110477

Contents lists available at ScienceDirect

Chinese Chemical Letters

journal homepage: www.elsevier.com/locate/cclet

Film thickness effect on 2D lead-free hybrid double perovskite properties: Band gap, photocurrent and stability

Mohamed Saber Lassoued [a,b], Faizan Ahmad [a,b], Yanzhen Zheng [a,b,*]

[a] School of Chemistry, State Key Laboratory of Electrical Insulation and Power Equipment, Xi'an Key Laboratory of Electronic Devices and Materials Chemistry, Xi'an Jiaotong University, Xi'an 710054, China
[b] Frontier Institute of Science and Technology, Xi'an Jiaotong University, Xi'an 710054, China

ARTICLE INFO

Article history:
Received 3 July 2024
Revised 18 September 2024
Accepted 19 September 2024
Available online 20 September 2024

Keywords:
Lead-free
Double perovskites
Film thickness
Photocurrent response
High stability

ABSTRACT

Lead-free hybrid double perovskites (LFHDPs) have received a lot of attention due to their environmental friendliness and promising attributes. However, studying the effect of film thickness on LFHDPs optoelectronic properties has not yet been investigated. Herein, we synthesized two new Ruddlesden–Popper LFHDPs, namely $(C_5H_{12}N)_4AgBiI_8$ (CAB-1) and $(C_6H_{14}N)_4AgBiI_8$ (CAB-2) using cyclopentylamine and cyclohexylamine as monoamine ligands. Indeed, these two Ag(I)-Bi(III) LFHDPs form smooth and uniform films ranging in thickness from 250 nm to 1 μm, with preferred orientations. Notably, the studies on the optical properties showed that the direct band gap value decreased from 2.17 eV to 1.91 eV for CAB-1 and from 2.05 eV to 1.86 eV for CAB-2 with increasing thickness. Accordingly, photo-current response using a xenon lamp revealed a significant difference of over 1000 nA between light and dark conditions for 1 μm-thickness films, suggesting potential for light harvesting. Other than that, thicker films of CAB-1 and CAB-2 exhibit high stability for 90 days in a relatively humid environment (RH of 55%), paving the way for promising optoelectronic applications.

Lead halide perovskite materials, have emerged as a remarkable group of semiconductors with tremendous potential for various optoelectronics, including solar cells and light-emitting diodes, as well as photodetectors and lasers [1-6]. In particular, three-dimensional halide perovskite materials, $CH_3NH_3PbI_3$, enjoy fascinating optoelectronic properties and have found widespread application, particularly in solar cells [7,8]. However, this intriguing compound still suffers from poor stability under moisture, oxygen, heat, or light. Indeed, the organic component (methylammonium) in the perovskite structure can degrade over time, leading to the formation of lead iodide and other decomposition products, which can significantly reduce device performance and lifespan [9,10]. Other than that, lead toxicity also presents a challenge for their widespread adoption and commercialization. In fact, during the manufacturing, disposal, and recycling processes, $CH_3NH_3PbI_3$ perovskites raise environmental and health concerns [11,12].

On the other hand, lead-free perovskites offer the potential to mitigate these concerns while retaining the advantageous optoelectronic properties that make perovskite materials attractive for various applications. In more detail, the monovalent replacement strategy, involving the substitution of lead (Pb^{2+}) with other monovalent metals such as Sn^{2+} and Ge^{2+}, has emerged as a promising approach for developing lead-free perovskite materials with favorable optical and electronic properties. Nevertheless, Sn- and Ge-based perovskites continue to be criticized for their instability, urging scientists to experiment with heterovalent replacements to synthesize chemically stable materials [13,14]. In order to maintain charge neutrality, the mixing of two heterovalent metals can be an effective strategy to substitute lead in halide perovskites. Within this approach, two metal cations combine to form an 'average' charge compared to conventional perovskites ($2M^{II} = M^{I} + M^{III}$), resulting in double perovskites. Since the early twentieth century, a significant number of double perovskites have indeed been crystallographically characterized or calculated, but their optoelectronic characterization and great promise for devices have lately been revisited. Several halide double perovskites have been reported in the literature showing interesting optoelectronic applications among them: $Cs_2AgBiBr_6$ is a halide double perovskite compound that has gained attention for its potential application in photovoltaic devices. It has the appropriate electrical and optical properties to be used as a light-absorbing substance in solar panels [15,16]. Further, another halide double perovskite, $Cs_2NaBiCl_6$, has indeed been investigated for use in semiconductor applications, such as photodetectors and

* Corresponding author.
E-mail address: zheng.yanzhen@xjtu.edu.cn (Y. Zheng).

https://doi.org/10.1016/j.cclet.2024.110477
1001-8417/

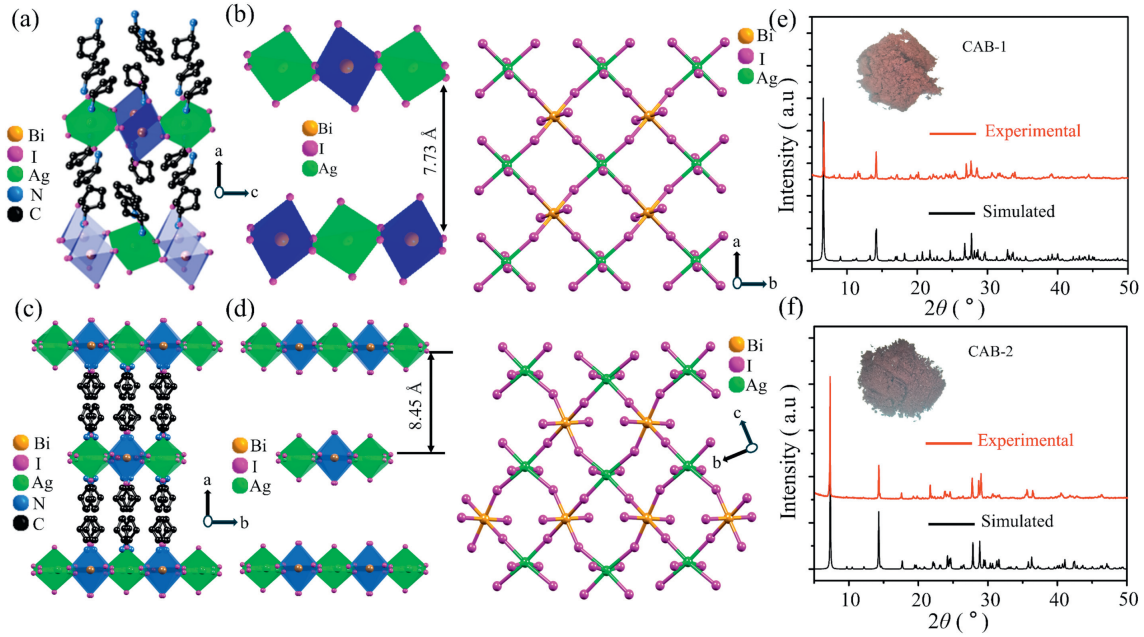

Fig. 1. The crystal structure of 2D hybrid layered hybrid double perovskite: (a) CAB-1 and (c) CAB-2 (hydrogens are omitted for clarity). The platform of inorganic layers consisting of alternate Ag–I_6 octahedrons and Bi–I_6 octahedrons of CAB-1 (b) and CAB-2 (d). Powder XRD patterns of CAB-1 (e) and CAB-2 (f).

light-emitting diodes (LEDs) [17-19]. By combining rubidium and copper in hydrobromic acid, a promising halide double perovskite has also been synthesized, Rb_2CuBr_3, showing potential applications in optical devices and optoelectronics. In fact, it exhibits intriguing properties, such as an X-ray imaging scintillator [20,21]. Following this interest, several groups have recently reported on the impacts of the dimensional reduction from 3D to 2D phases of the aforementioned double perovskites. To the best of our knowledge, many Ruddlesden–Popper and Dion–Jacobson type hybrid double perovskites have been synthesized with various chemical compositions ($M^I = Cu^+$, Ag^+, Au^+, Na^+, and K^+, and $M^{III} = In^{3+}$, Sb^{3+}, Bi^{3+}, Tl^{3+}, Au^{3+}, Y^{3+}, and Gd^{3+}) and showed intriguing properties [22-30]. Zheng *et al.* reported five new Bi/Cu two-dimensional Dion Jacobson or Ruddlesden-Popper iodides hybrid double perovskites. These perovskites showed narrow band gaps and excellent stability [31]. Another interesting work was reported by Zhang *et al.*, whose synthesized ferroelectric halide double perovskites, (4,4-difluoropiperidinium)$_4$AgBiI$_8$, exhibited a high Curie temperature (T_c) of 422 K, large polarization (Ps = 10.5 μC/cm^2) [32]. However, the number of experimentally synthesized LFHDPs remains low when compared to their single-metallic counterparts. Furthermore, no studies focusing on the effect of film thickness on LFHDPs properties has been reported to date.

In the light of this discussion, we reported two new Ruddlesden-Popper 2D hybrid double perovskites of formula $(C_5H_{12}N)_4AgBiI_8$ (CAB-1) and $(C_6H_{14}N)_4AgBiI_8$ (CAB-2). Importantly, adequate surface coverage films of both compounds are fabricated and exhibited, narrow band gaps, high photocurrent and excellent stability under humid conditions with increasing thickness. To the best of our knowledge, this is the first study to investigate the effect of film thickness on LFHDPs optoelectronic properties.

Single crystals of CAB-1 and CAB-2 were prepared using a simple one-pot hydrothermal process in which a hydroiodic acid solution containing stoichiometric amounts of BiI_3, AgI, and cyclopentylamine (CPA) or cyclohexylamine (CHA) was heated at 150 °C for 10 h. More information is provided in Supporting information. Figs. S1a and S2a (Supporting information) depict the morphology of CAB-1 and CAB-2 using scanning electron microscopy, revealing a single millimetric crystal with a net surface. Furthermore, through elemental mapping of CAB-1 and CAB-2 single crystals, we found that Ag, Bi, I, C, and N are homogeneous and evenly distributed (Figs. S1b-f and S2b-f in Supporting information).

Single-crystal X-ray diffraction measurements were performed at 150 K to reveal the crystal structures of CAB-1 and CAB-2. Indeed, CAB-1 crystallized in a monoclinic system with a centrosymmetric (*P 12$_1$/c 1*) space group with the following cell parameters: $a = 9.0100(1)$ Å, $b = 9.0102(8)$ Å, $c = 24.001(3)$ Å, and $\beta = 90.016(6)°$ (Table S1 in Supporting information). The asymmetric unit consists of Bi(III) and Ag(I) cations, two protonated cyclopentylammonium, and four iodide anions (Fig. S3a in Supporting information). Figs. 1a and b show that the crystal structure of the 2D $[AgBiI_8]_n^{4n-}$ inorganic framework alternates with two organic layers (cyclopentylammonium cations). Indeed, $[AgBiI_8]_n^{4n-}$ layers were formed using Ag–I–Bi bridges to design vertex-sharing $[AgI_6]$ and $[BiI_6]$ octahedra.

Table S2 and Fig. S3b (Supporting information) show that the bond length of Bi-I in the $[BiI_6]$ octahedron is relatively consistent, with distances ranging from 3.0603(6) Å to 3.0887(7) Å. While bond angles varied between 88.708(17)° and 180° (I_{eq}–Bi–I_{eq} (eq means equatorial) angles ranged from 88.708(17)° and 91.291(17)° and I_{ax}–Bi–I_{ax} (ax means axial) angles are 180.00°) indicating the slight distortion $[BiI_6]$ octahedral. Nevertheless, concerning $[AgI_6]$ octahedra, the bond distances of Ag-I differ significantly. In fact, the two axial Ag-I bonds' lengths range between 2.6775(7) Å and 2.6776(7) Å. However, the four equatorial Ag-I bond lengths are showing considerable elongation compared to their axial counterparts and range between 3.3349(6) Å and 3.5125(8) Å. I_{eq}–Ag–I_{eq} and I_{ax}–Agi–I_{ax} angles varied from 89.840(19)° to 90.159(19)° and 177.80(3)° to 180°, respectively. Here, it is obvious that $[AgI_6]$ octahedra exhibit significant distortion rather than their $[BiI_6]$ counterpart. In contrast, CAB-2 crystalizes in the monoclinic *C12/c1* space group after replacing cyclopentylamine with cyclohexylamine (Table S1). Similar to CAB-1, the asymmetric unit of CAB-2 consists of one Bi(III) ion, one Ag(I) ion, four iodide anions, and two protonated organic cations (Fig. S4a in Supporting information). The crystal structure is represented by a single-layer perovskite with an orderly arrangement of $[AgBiI_8]_n^{4n-}$ isolated

by organic cations (Figs. 1c and d). The Bi-I distance ranges from 3.0645(19) Å to 3.094(2) Å, indicating that the [BiI_6] octahedron exhibits minimal distortion (Table S3 and Fig. S4b in Supporting information). In the [AgI_6] octahedron, the two apical Ag-I_{ax} bond lengths (2.692(2) Å) are significantly shorter than the remaining four Ag-I distances (3.195(4) Å to 3.8664(38) Å) in the layer. The I-Bi-I and I-Ag-I angles vary from 87.32(5)° to 180° and 84.128(66)° to 172.63(45)° respectively (Table S3 in Supporting information). To provide further information about the distortion of bond distances distortion within [AgI_6] and [BiI_6] octahedra in CAB-1 and CAB-2, the degree of deviation of bond lengths was determined and discussed (Table S4 in Supporting information).

Interestingly, due to their distorted geometry, cyclohexylammonium and cyclopentylammonium can firmly support the inorganic layer and play a key role in the formation of two-dimensional hybrid double perovskites. In fact, cyclohexylammonium and cyclopentylammonium have regular spatial configurations, with normal C-C and C-N distances between 1.418(19) Å and 1.55(6) Å and C-C-C and C-C-N angles between 103.2(12)° and 114.0(11)° (Tables S2 and S3). Furthermore, CAB-1 and CAB-2 show many intermolecular hydrogens bond contacts between $[(C_5H_{12}N_2)_2]^{2+}$ or $[(C_6H_{14}N_2)_2]^{2+}$ cations and $[AgBiI_8]^{4-}$ anions, which are playing an important role in stabilizing structures (Tables S5 and S6, and Figs. S3c and S4c in Supporting information). The abundance of hydrogen bonds in both hybrid double perovskites and the nature of these liaisons have also been calculated using molecular Hirshfeld surfaces (MHS) analysis (Fig. S5 in Supporting information). More information is provided in Supporting information.

To check the stability and verify the homogeneity of these hybrid double perovskites, we measured powder XRD of both samples. As shown in Figs. 1e and f, we note a coincidence between experimental patterns and simulated ones for CAB-1 and CAB-2, indicating the high stability of these two perovskites under ambient environmental conditions. Furthermore, energy-dispersive spectroscopy (EDS) of CAB-1 and CAB-2 powder, confirmed the presence of Ag, Bi, I, C, and N (Figs. S6a and b in Supporting information).

Film preparation has a significant impact on the performance and reliability of semiconductor materials used in optoelectronic devices. Intriguingly, the obtained 2D bismuth/silver iodides hybrid double perovskites can grow easily into glass/ITO substrates using spin coating method. Further information can be found in Supporting information. Indeed, spin coating ensures the fabrication of films with exceptional uniformity and offers precise control over the thickness to meet specific requirements to be employed in photonic devices. Hence, a series of perovskite films with different thicknesses of 250 nm, 500 nm, and 1 µm have been prepared by simple adjusting of spin speed and solution concentration (Figs. 2a, c, e and g and Figs. S7a-c in Supporting information). As shown in Figs. S8a, S9a, S10a, S11a, S12a, and S13a (Supporting information), scanning electron microscopy (SEM) images reveal that all CAB-1 and CAB-2 films with different thicknesses are homogeneous, smooth, and pinhole-free. Here, we need to mention that some valleys appeared in the film surfaces of CAB-1 (250 nm) and CAB-2 (250 nm), which is due to the influence of solvent removal.

To further check the homogeneity of CAB-1 and CAB-2 films, we studied the distribution of their constituting elements in the surface using elemental mapping and EDS. We noticed that Ag, Bi, I, C, and N are uniformly and evenly distributed and matched precisely with theoretical values (Table S7 and Figs. S8b-f, S9b-f, S10b-f, S11b-f, S12b-f, S13b-f, and S14 in Supporting information). In addition, understanding the growth orientation of 2D-layered perovskites can significantly impact the optical, electronic, and structural properties of the material. As a result, by studying the conspicuous peaks in the XRD spectra of thin films containing CAB-1 and CAB-2, we can determine the orientation of the polycrystals within the films relative to the substrate. As shown in Figs. 2b, d, f and h and Figs. S7b and d (Supporting information), we note the presence of principal reflection planes (002) and (200) for CAB-1 (250 nm, 500 nm, and 1000 nm) and CAB-2 films (250 nm, 500 nm, and 1000 nm), respectively, indicating that crystalline structures are growing vertically toward the substrate, which directly impacts the optical characteristics of perovskite materials (Figs. 2i and j). Thus, it is important to study the effect of film thickness on CAB-1 and CAB-2 optoelectronic properties (*vide-infra*).

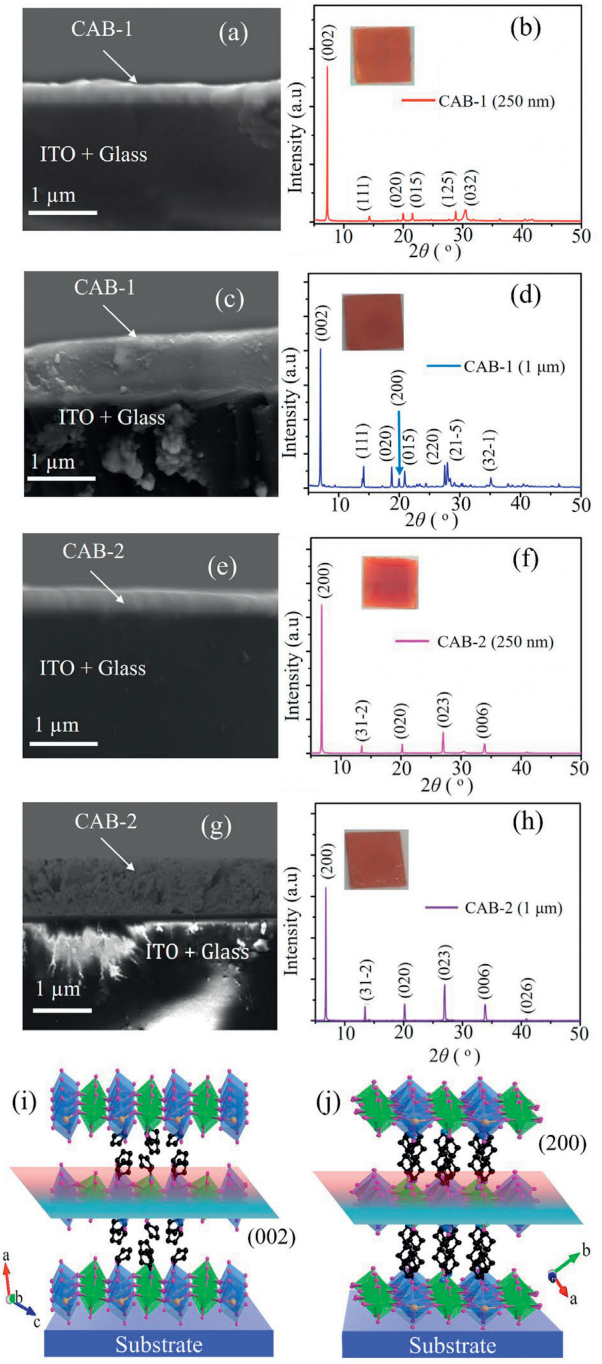

Fig. 2. Cross-sectional SEM images of different-thickness films made from CAB-1 (a, c) and CAB-2 (e, g). Film XRD patterns for CAB-1 (b, d) and CAB-2 (f, h) for different thickness films. Inset: Photograph of the films of CAB-1 and CAB-2. Illustration of CAB-1 (i) and CAB-2 (j) films with respect to the substrate.

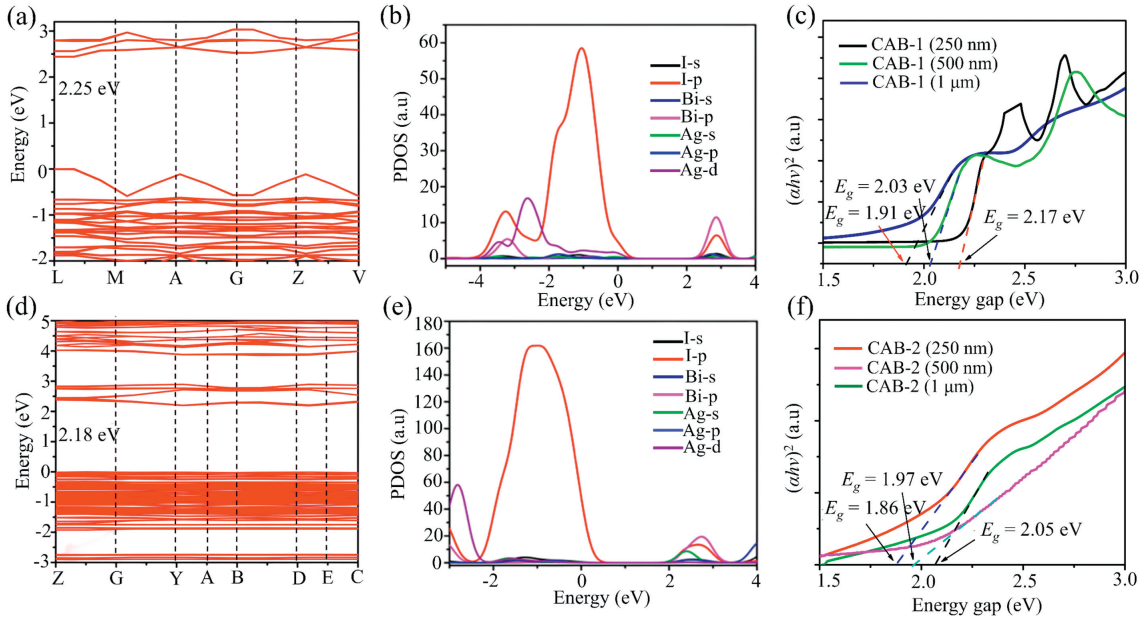

Fig. 3. DFT-GGA-PBE band structures of CAB-1 (a) and CAB-2 (d). Partial density of states of CAB-1 (b) and CAB-2 (e). The UV–vis absorbance spectra of film samples of CAB-1 (c) and CAB-2 (f) show the optical band gaps.

To advance our understanding of these two hybrid double perovskite materials and optimize their performance for various optoelectronic applications, we measured the absorption band edges and band gaps of CAB-1 and CAB-2 using powder samples and films with different thicknesses. Here, we used Kubelka-Munk function ($F(R) = aS^{-1} = (1\text{-}R)^2/(2R)$, where "*R*" is the diffuse reflectance of the material, expressed as a fraction between 0 and 1, "*a*" is the absorption coefficient, and "*S*" is the scattering coefficient) to convert the diffuse reflectance spectrum into absorbance spectrum [33,34].

According to Fig. S15a (Supporting information), the absorption of CAB-1 and CAB-2 powders is 647 nm and 670 nm, respectively. Direct fitting scenarios were used to determine the band gaps, as illustrated in Fig. S15b (Supporting information), CAB-1 and CAB-2 have band gaps of 1.89 eV and 1.83 eV, respectively, indicating their dark-red color. Furthermore, their band gaps are arranged in the same order as Ag-I-Bi bond angles, with the smallest angle corresponding to the smallest band gap. This trend was also confirmed *via* DFT calculations (see *infra*). To perform theoretical simulations, we used first-principles simulation with the Material Studio 2019 package's CASTEP code. Indeed, for self-consistent DFT calculations, we used the GGA-PBE exchange-correlation functional rather than spin orbital coupling (SOC) (see Supporting information for details). Generally, the theoretical calculations closely matched the experimental data. The theoretical band gaps of monolayered CAB-1 and CAB-2 are 2.25 eV and 2.18 eV, respectively (Figs. 3a and d). Moreover, valence band minimum (VBM) and conduction band maximum (CBM) for CAB-1 and CAB-2 are pointing at the same point L and Y, respectively, which are reflective of their direct band gap. Furthermore, to investigate the bandgap nature of CAB-1 and CAB-2, we calculated the partial density of states (PDOS) near band gaps. We found that the CBM is dominated by Bi-6p and I-4p, while the VBM is determined by Ag-4d and I-4p states (Figs. 3b and e).

In other hand, to check the suitability of CAB-1 and CAB-2 to be used in optoelectronic devices, we studied the effect of film thickness on the optical properties of CAB-1 and CAB-2. As shown in Fig. 3c, the band gap energy of CAB-1 decreases from 2.17 eV to 1.91 eV with varying thickness from 250 nm to 1 μm. Likewise, CAB-2 showed similar behavior with varying film thickness. Indeed, as shown in Fig. 3f, CAB-2 energy gaps decreased from 2.05 eV for 250 nm film thickness, to 1.86 eV for 1 μm film thickness. Herein, it is obvious that film thickness plays an important role in regulating band gaps. Indeed, thicker films generally have fewer surface defects per unit volume and a lower surface-to-volume ratio, resulting in a more relaxed lattice that resembles the bulk material, which can result in a narrower band gap.

To determine the effect of film thickness on the photoelectric behavior of CAB-1 and CAB-2, as well as to further investigate their optoelectronic application potential, we measured the photo-conductivities of both hybrid double perovskites using film samples with different thicknesses as active layers under 350 W Xenon lamp irradiation at 0.8 V bias (more information can be found in Supporting information).

As shown in Figs. 4a and b, Figs. S16a and b, S17a and b (Supporting information), CAB-1 and CAB-2 have a low dark current, when using a 250 nm and 500 nm film thicknesses, while under illumination, the photocurrent begins to increase and eventually reaches approximately twice and three times that of the dark current. In contrast, by measuring 1 μm of film thickness, the current was raised to 5-fold and 6-fold, respectively. Indeed, at bias voltage of 0.8 V, the current of CAB-1 and CAB-2 with 250 nm thickness increased from 0.34×10^{-6} A/cm^2 (dark) to 0.79×10^{-6} A/cm^2 (light) and from 0.41×10^{-6} A/cm^2 (dark) to 0.98×10^{-6} A/cm^2 (light), respectively. While for 500 nm CAB-1 and CAB-2 film thickness, the current rose from 0.31×10^{-6} A/cm^2 to 1.02×10^{-6} A/cm^2 and from 0.51×10^{-6} A/cm^2 to 1.55×10^{-6} A/cm^2 for CAB-1 and CAB-2, respectively.

However, with 1 μm film thickness, the current was improved from 0.33×10^{-6} A/cm^2 (dark) to 1.54×10^{-6} A/cm^2 (light) for CAB-1 and from 0.35×10^{-6} A/cm^2 (dark) to 1.95×10^{-6} A/cm^2 (light) for CAB-2. These values are greater than those of the majority lead-free halide organic-inorganic reported materials (Table S8 in Supporting information). Herein, it is obvious that thick perovskite layers can absorb more incident light due to multiple light scattering events within the thicker absorber layer, potentially improving photon absorption. Alternatively, as shown in Figs. 4c and d, these two hybrid double perovskites demonstrated repeatable and regular switching (on/off) of the light, demonstrating the high stability of CAB-1 and CAB-2.

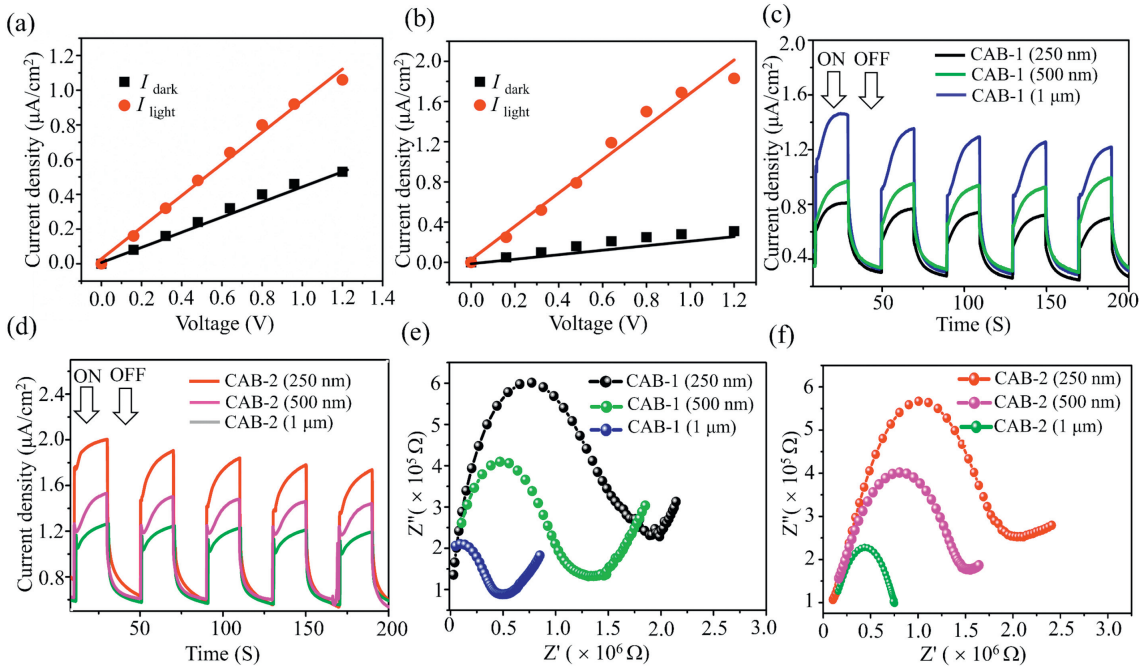

Fig. 4. *I–V* plots for dark and light currents of CAB-1 (250 nm) (a), CAB-1 (1000 nm) (b) measured at 298 K. *I–t* plots of several irradiation cycles of CAB-1 (c) and CAB-2 (d). EIS Nyquist plots of CAB-1 (e) and CAB-2 (f).

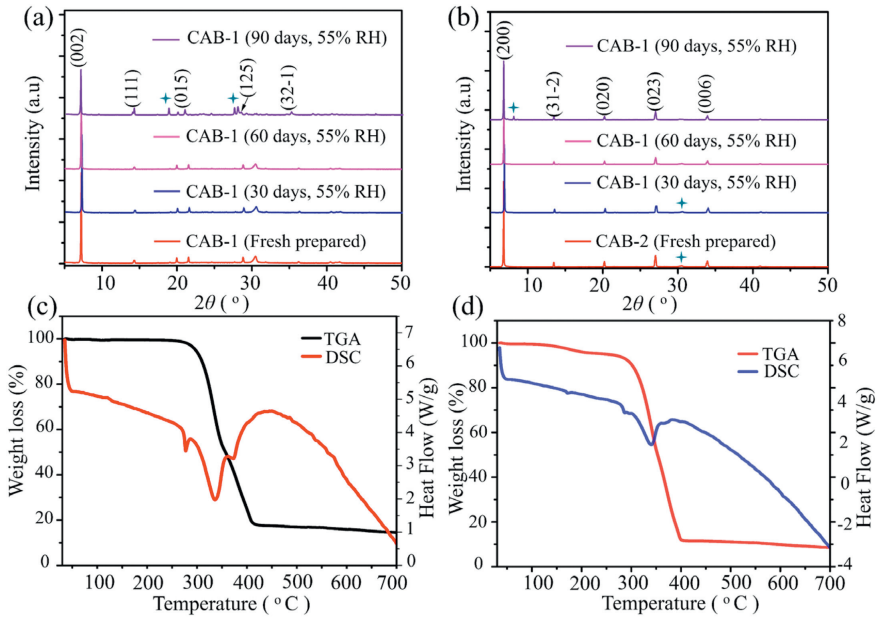

Fig. 5. XRD patterns of CAB-1 (250 nm) (a) and CAB-2 (250 nm) (b) films before and after exposure to humidity (55% RH) at different times. TGA curves of CAB-1 (c) and CAB-2 (d) powders.

To confirm the above results, electrochemical impedance spectroscopy (EIS) tests were conducted (Figs. 4e and f) to gain a thorough understanding of the separation efficiency of photogenerated electron-hole pairs in CAB-1 and CAB-2. According to the Nyquist plots, the diameter of the plot of CAB-1 and CAB-2 with 1000 nm thickness was significantly smaller than that of CAB-1 and CAB-2 with 500 nm and 250 nm film thickness, indicating their better carrier separation ability [35,36].

Film stability is of paramount importance for perovskite materials due to its direct impact on the performance, reliability, and commercial viability of perovskite-based devices. Since the first fabrication of a primary solar cell device in 2009, researchers have paid much attention to improving the stability of perovskite materials. To assess the stability of these 2D double structures, we first stored film samples of CAB-1 and CAB-2 of varying thicknesses under 55% humidity for three successive months. We remark that thicker films of CAB-1 (1 μm) and CAB-2 (1 μm) exhibit high moisture stability after three months of storage, still maintaining their original phase and structural integrity over a long period of time, indicating their excellent stability (Figs. S18a and b in Supporting information). By contrast, we note a start of decomposition for CAB-1 and CAB-2 films with 250 nm: Indeed, we note the appearance of two new peaks at 19° and 27° after 3 months of storage of CAB-1 at 55% humidity compared

to fresh-prepared film (Fig. 5a). Meanwhile, for CAB-2, we record first the existence of a new peak at 8° and the disappearance of peak at 30°, which proves the launch of degradation (Fig. 5b). Here, it is obvious that thicker LFHDPs films offer better resistance to environmental factors such as moisture induced degradation, potentially enhancing device stability and long-term performance.

On the other hand, we conducted thermogravimetric analyses (TGA) for CAB-1 and CAB-2 powder samples between 30 °C and 700 °C under nitrogen atmosphere. The TGA results show that all of the compounds are resistant to high temperatures and have relatively good thermal stability, with no significant mass loss occurring until the temperature reaches at least 280 °C (Figs. 5c and d).

To summarize, we have successfully prepared and studied the effect of film thickness on RP 2D Bi/Ag based double perovskites CAB-1 and CAB-2. Interestingly, both hybrid double perovskites can form smooth and uniform films with different thicknesses varying from 250 nm to 1 μm. By measuring the electronic properties of CAB-1 and CAB-2 film band gaps reduced from 2.17 eV, to 1.91 eV and 2.05 eV to 1.86 eV, respectively, by increasing thickness. Accordingly, thicker LFHDPs films absorb more incident light (∼1000 nA between I_{light} and I_{dark}) due to multiple light scattering events, potentially improving photon absorption. Furthermore, CAB-1 and CAB-2 (1 μm film thickness) are more resistant to humid environments (55% RH), potentially improving device stability and long-term performance. Hence, this study provided an insight about adequate lead-free hybrid double perovskite films can be used to fabricate optoelectronic devices.

Declaration of competing interest

The authors declare that they have no known competing financial interests or personal relationships that could have appeared to influence the work reported in this paper.

CRediT authorship contribution statement

Mohamed Saber Lassoued: Writing – review & editing, Writing – original draft, Software, Funding acquisition, Data curation. **Faizan Ahmad:** Writing – review & editing, Visualization, Software. **Yanzhen Zheng:** Writing – review & editing, Validation, Supervision, Project administration, Funding acquisition.

Acknowledgments

This work was supported by the National Natural Science Foundation of China (Nos. 22375157 and W2433042), the Key Scientific and Technological Innovation Team of Shaanxi Province (No. 2020TD-001), the Fundamental Research Funds for Central Universities, State Key Laboratory of Electrical Insulation and Power Equipment (No. EIPE23409) and the Instrument Analysis Center of Xi'an Jiaotong University for assistance.

Supplementary materials

Supplementary material associated with this article can be found, in the online version, at doi:10.1016/j.cclet.2024.110477.

References

[1] B. Zhao, Y. Lian, L. Cui, et al., Nat. Electron. 3 (2020) 704–710.
[2] S.D. Stranks, H.J. Snaith, Nat. Nanotechnol. 10 (2015) 391–402.
[3] L. Lei, Q. Dong, K. Gundogdu, F. So, Adv. Funct. Mater. 31 (2021) 2010144.
[4] F. Deschler, M. Price, S. Pathak, et al., J. Phys. Chem. Lett. 5 (2014) 1421–1426.
[5] J. Miao, F. Zhang, J. Mater. Chem. C 7 (2019) 1741–1791.
[6] S. Kar, N.F. Jamaludin, N. Yantara, S.G. Mhaisalkar, W.L. Leong, Nanophotonics 10 (2020) 2103–2143.
[7] K.T.A. Kojima, Y. Shirai, T. Miyasaka, J. Am. Chem. Soc. 131 (2009) 6050–6051.
[8] Best Research-Cell Efficiency Chart (National Renewable Energy Laboratory (2024) accessed 22 May https://www.nrel.gov/pv/cell-efficiency.html .
[9] L. Etgar, Energy Environ. Sci. 11 (2018) 234–242.
[10] B.W. Park, S.I. Seok, Adv. Mater. 31 (2019) 1805337.
[11] S. Chen, Y. Deng, H. Gu, et al., Nat. Energy. 5 (2020) 1003–1011.
[12] X. Li, F. Zhang, J. Wang, et al., Nat. Sustainability 4 (2021) 1038–1041.
[13] D. Ray, C. Clark, H.Q. Pham, et al., J. Phys. Chem. C 122 (2018) 7838–7848.
[14] E.S. Parrott, R.L. Milot, T. Stergiopoulos, et al., J. Phys. Chem. Lett. 7 (2016) 1321–1326.
[15] C. Wu, Q. Zhang, Y. Liu, et al., Adv. Sci. 5 (2018) 1700759.
[16] H. Lei, D. Hardy, F. Gao, Adv. Funct. Mater. 31 (2021) 2105898.
[17] J. Jiang, G. Niu, L. Sui, et al., J. Phys. Chem. Lett. 30 (2021) 7285–7292.
[18] A. Karmakar, G.M. Bernard, A. Pominov, et al., J. Am. Chem. Soc. 8 (2023) 4485–4499.
[19] J.D. Majher, M.B. Gray, T.A. Strom, P.M. Woodward, Chem. Mater. 5 (2019) 1738–1744.
[20] H. Wang, J.X. Wang, X. Song, et al., ACS Cent. Sci. 9 (2023) 668–674.
[21] B. Yang, L. Yin, G. Niu, et al., Adv. Mater. 31 (2019) 1904711.
[22] X.J. Liu, K. Matsuda, Y. Moritomo, A. Nakamura, N. Kojima, Phys. Rev. B: Condens. Matter Mater. Phys. 59 (1999) 7925–7930.
[23] F. Wei, Z. Deng, S. Sun, et al., Mater. Horiz. 3 (2016) 328–332.
[24] Z. Deng, F. Wei, S. Sun, et al., J. Mater. Chem. A 4 (2016) 12025–12029.
[25] Z. Deng, F. Wei, F. Brivio, et al., J. Phys. Chem. Lett. 8 (2017) 5015–5020.
[26] M.S. Lassoued, L.Y. Bi, Z. Wu, G. Zhou, Y.Z. Zheng, J. Mater. Chem. C 8 (2020) 5349–5354.
[27] M.S. Lassoued, T. Wang, Q.W. Li, et al., Mater. Chem. Front. 6 (2022) 2135–2142.
[28] M.S. Lassoued, T. Wang, A. Faizan, et al., J. Mater. Chem. C 10 (2022) 12574–12581.
[29] Q.W. Li, M.S. Lassoued, W.P. Chen, G.Y. Gou, Y.Z. Zheng, ACS Appl. Mater. Interfaces 16 (2024) 5769–5778.
[30] Q.W. Li, L.Y. Bi, M.S. Lassoued, et al., Nanoscale 15 (2023) 5265–5273.
[31] L.Y. Bi, T.L. Hu, M.Q. Li, et al., J. Mater. Chem. A 8 (2020) 7288–7296.
[32] C.F. Wang, H. Li, M.G. Li, et al., Adv. Funct. Mater. 31 (2021) 2009457.
[33] P. Kubelka, F. Munk, Z. Techn. Physik. 12 (1931) 593–601.
[34] J. Tauc, Mater. Res. Bull. 5 (1970) 721–729.
[35] S. Yang, C. Liu, H. Li, et al., Energy Storage Mater. 39 (2021) 278–286.
[36] L. Xia, W. Zhou, Y. Xu, et al., Chem. Eng. J. 451 (2023) 138747.